NANO LETTERS

2008
Vol. 8, No. 6
1610-1618

DNA Transport in Hierarchically-Structured Colloidal-Nanoparticle Porous-Wall Nanochannels

Deying Xia,[†] Thomas C. Gamble,[‡] Edgar A. Mendoza,[§] Steven J. Koch,[†,||] Xiang He,[†] Gabriel P. Lopez,[‡] and S. R. J. Brueck*[,†,⊥]

Center for High Technology Materials, University of New Mexico, 1313 Goddard, SE, Albuquerque, New Mexico 87106, Center for Biomedical Engineering and Department of Chemical and Nuclear Engineering, Department of Physics and Astronomy, Department of Electrical and Computer Engineering, University of New Mexico, Albuquerque, New Mexico 87131, Redondo Optics Inc., 811 N. Catalina Avenue, Suite 1100, Redondo Beach, California 90277

Received January 20, 2008; Revised Manuscript Received April 1, 2008

ABSTRACT

We report a simple approach to the formation of 3D colloidal nanoparticle structures incorporating enclosed mesoscopic structures through a simple process of spin-coating-driven directed self-assembly onto lithographically defined polymer templates. Removal of the buried polymer patterns by high temperature calcination results in the formation of hierarchically enclosed channels, continuous networks, isolated cavities, and multilayered structures with high stability and environmental resistance. These channels are used to investigate the transport of DNA molecules in constrained geometries.

An exciting direction for nanoparticle structures is the fabrication of complex three-dimensional (3D) hierarchical structures with potential applications to multilayer photonic crystals, chemical sensors, catalysis, and biotechnology. Micro- and nanoparticles have been used as templates for preparation of porous metallic nanostructures and monodisperse colloidal crystals.[1,2] Directed self-assembly of metal nanoparticles (e.g., Au) into alumina membranes forms porous metallic tubes.[3] The fabrication of spherical, cylindrical, and hollow colloidal crystals using spray and microcapillaries has also been studied using template-assisted approaches.[4–7] Three-dimensional periodic structures with micrometer-scale periods have been fabricated with nanoparticle inks.[8] Well-defined 3D and multiplayer nanostructures with deposited metal (Au) have been formed by a nanotransfer printing approach.[9,10] Even though nanochannel structures for nanofluidic applications have been fabricated using traditional etching and thermal oxidation approaches using both interferometric and nanoimprint lithographies,[11–13] there have been relatively few reports of the fabrication of enclosed mesoscopic structures using nanoparticles as building blocks, thereby providing porous confinement layers around the voids.[14] These structures have evident biomimetic organization (similar to trees, skin, hair, etc.) with long transport channels interconnected by porous media along with hierarchical structures for fluid access that will be important both for laboratory studies of biological processes and for biomimetic applications.

Directed self-assembly, the combination of bottom-up self-assembly and top-down pattern definition, is a promising approach for the fabrication of complex micro- and nanostructures.[15,16] Generally, and in this work, mesoscopic enclosed structures (≫particle diameter) have been defined by lithographic techniques while the nanoscale interparticle separations giving rise to the porosity (≪particle diameter) are generated through self-assembly approaches.

In previous work, we demonstrated 1D and 2D patterned nanoparticle structures on flat and patterned surfaces using directed self-assembly.[17,18] Here, we present an approach for fabrication of enclosed mesoscopic silica nanoparticle structures on planar Si surfaces using simple and inexpensive

* Corresponding author. E-mail: brueck@chtm.unm.edu.
[†] Center for High Technology Materials, University of New Mexico.
[‡] Center for Biomedical Engineering and Department of Chemical and Nuclear Engineering.
[§] Redondo Optics Inc.
[||] Department of Physics and Astronomy, University of New Mexico.
[⊥] Department of Electrical and Computer Engineering, University of New Mexico.

10.1021/nl080190s CCC: $40.75 © 2008 American Chemical Society
Published on Web 05/07/2008

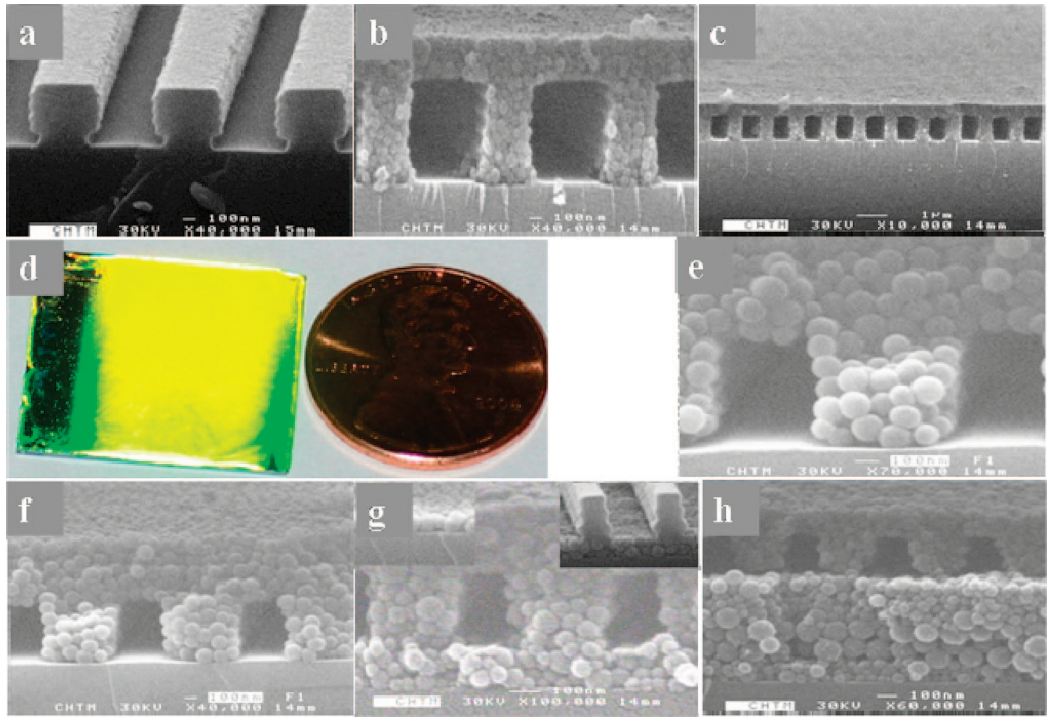

Figure 1. One-dimensional enclosed channels with silica particles. (a) SEM image of 1D channel with negative PR 500P. (b−c) 1000 nm period channels formed with 50 nm silica nanoparticles. (d) Photograph of a typical, 2 × 2 cm^2, 1D channel sample showing uniformity. (e−f) SEM images of 1D channels with negative PR 500P, 1000 nm period, and 160 nm silica particle. (g) SEM image of enclosed channel structures with 50 nm silica particles on all sides, with 500 nm periods atop a two-layer silica nanoparticle blanket film: (top left) monolayer film of 50 nm silica nanoparticles; (top right) PR/wet-I patterns atop a two-layer 50 nm silica nanoparticle film. (h) SEM image of enclosed channels with 500 nm periods on heterogeneous 50/160/50 nm silica particle films.

approaches including spin-coating and interferometric lithography (IL). This approach provides a flexible, rapid, and inexpensive fabrication suite, using only low-cost and large-area lithography techniques while avoiding costly and complex processing steps such as etching and metallization. Photoresist (PR) patterns defined by interferometric lithography were used as a soft template around which silica nanoparticles were self-assembled. Additional structure at larger scales can be added, either in the same or different resist levels, using traditional mix-and-match lithographic processes. Multiple layer stacks, as high as four photoresist layers, are demonstrated, allowing complex functionality. High-temperature calcination was used to remove the PR and enhance the structural stability of the nanoparticle assembly by strengthening the bonding between adjacent particles (localized sintering or necking). Using this approach, the fabrication of complex 3D structures incorporating defined length scales over a 10^7 scale range from ~5 nm to 2 cm is demonstrated. The hierarchical integrated organization provides for facile interfacing between macro- and nanoscales.

IL is a powerful technique for fabrication of a wide range of samples.[19] IL is a parallel optical lithography approach that provides an inexpensive, large-area capability (typical samples in this work were ~2 × 2 cm^2). In conventional photolithography, the time and cost required to fabricate a photomask can be a significant issue, particularly for dense nanoscale features patterned by e-beam lithography. IL does not require a photomask, with the tradeoff of reduced pattern flexibility (periodic patterns) for individual layers.[15] Mix-and-match lithographic approaches with lower resolution tools can provide some of the requisite pattern flexibility. There are many active research areas for the applications of IL technology such as fabrication of photonic crystals for the visible spectrum[20] and metamaterial structures exhibiting a negative permeability and negative refractive index.[21,22]

Silica nanoparticles are commercially available, easy to prepare, compatible with both silicon microfabrication and biological species, and easy to functionalize. In addition, the use of silica nanoparticles for providing the walls (and tops) of enclosed channels is very attractive for biological applications due to their extended optical transparency range (UV−THz).[11]

Several examples of 1D enclosed nanostructures are shown in Figure 1. A colloidal suspension of 50 nm diameter silica nanoparticles was used to form 1D enclosed channels with an ~1 μm period as shown in Figure 1a−d. Well-defined, 1D stacked PR/antireflection coating (ARC) polymer patterns were generated with IL using negative PR and a developable ARC (Figure 1a). After six cycles of spin-coating with a dilute aqueous silica suspension (2 wt %) and removal of the PR and ARC by high temperature calcination, relatively large channels (~700 nm wide) were fabricated with high fidelity to the PR/ARC templates (Figure 1b−c). Smaller cross section nanochannels are readily available, as will be demonstrated below. One important advantage of this approach for forming the enclosed nanostructures is the uniformity over a large area. The typical size of a Si wafer

sample was 2 × 2 cm^2 as shown in Figure 1d. A uniform yellow diffraction color was observed with white-light, tilted-angle illumination, indicating a uniform array of nanostructures; detailed SEM measurements confirm this result.

Larger diameter (∼160 nm) silica particles were used to form enclosed channels with a ∼1 μm period using negative PR 500P. The channels have a 600 × 500 nm^2 cross section (Figure 1e). The silica particle array structure with these larger and more nearly monodisperse particles is hexagonal close-packed. The top seal layer has roughly five layers of silica particles (Figure 1f). We can extend this approach to particle sizes large enough to directly form photonic crystals. The lithography methods used for this purpose can be IL or conventional photolithography. Fabrication of buried linear and three-dimensional extrinsic defects within self-assembled colloidal photonic crystals has been demonstrated recently via a directed self-assembly strategy involving a combination of top-down photolithography and bottom-up colloidal assembly.[23,24]

Furthermore, enclosed channel structures with nanoparticles on all four sides can be fabricated (Figure 1g−h). To form this structure, a blanket film (monolayer or multiple layer) of silica particles was first assembled on a flat sample surface using spin-coating deposition with appropriate diluted silica particle suspensions. A monolayer film of ∼50 nm diameter silica nanoparticles was deposited on a planar Si surface with ∼2 wt % suspension (top left inset in Figure 1g). Therefore, approximately two-layer-deep silica particle arrays were formed with a two-step deposition under these same conditions. The IL defined PR/ARC patterns were formed atop the self-assembled silica nanoparticle films.[25,26] In this case, using a positive PR (top right insert in Figure 1g). Well-defined enclosed channels with silica particles on all sides are clearly observed with high fidelity to the PR/ARC patterns. Free-standing channel structures can also be fabricated with a metal layer, such as Cr, or other release layer between the Si substrate and the silica particle layer.[27]

Finally, heterostructure colloidal crystal films can be formed by varying the particle properties (size, composition) within the multiple colloidal nanoparticle deposition stages. This possibility is demonstrated by Figure 1h. The structure on the bottom is composed of a heterogeneous colloidal crystal (50/160/50 nm diameters) on a Si substrate. Two layers of 160 nm diameter silica particles are sandwiched between 50 nm diameter silica colloidal films. Similar composite structures (Figure 1h) have been obtained previously by convective deposition using two different sphere sizes.[28] These channel structures with silica nanoparticles on all sides confirm the extensibility and suitability of this approach to the fabrication of linear extrinsic defects (waveguides) for colloidal nanoparticle photonic crystal applications.[24]

High temperature calcination (∼700−1000 °C in air ambient) was used to remove the sacrificial PR and ARC patterns and to enhance the mechanical strength of the resultant channel structures by sintering of the silica spheres in the immediate vicinity of the nanoparticles contact points. The ordering and porosity of silica nanoparticle films decrease when going from the low to high temperature.[7] At the highest temperatures investigated, coalescence of the nanoparticles occurs. The silica nanoparticle melting point was reduced substantially from that of an amorphous bulk material (1986 K).[29]

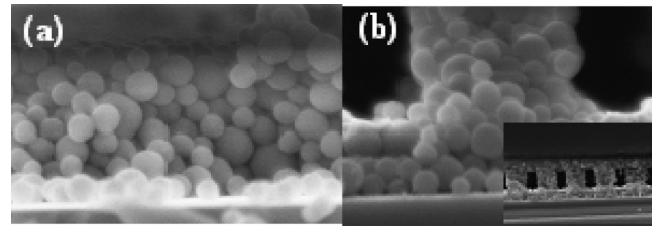

Figure 2. High-resolution SEM images of 50 nm silica nanoparticle film and channel structure. (a) Films after baking in air at 115 °C for 3 min. (b) Channel structure after 800 °C 2 h calcination (bottom right insert: large area image).

The samples treated at T < 700 °C present a much lower mechanical stability than those annealed at T ∼ 950 °C. The formation of necks between the spheres caused by an incipient sintering process starts taking place at T ∼ 800 °C through viscous flow and is responsible for the sample strengthening.[30] When samples are annealed at T > 950 °C, the nanoparticle spheres deform, losing their spherical shape. Investigating the temperature effects on enclosed channel structures, we draw a similar conclusion to that of Miguez[31] that the mechanical strength of channel structures was low after calcination at $T \lesssim$ 700 °C. We also tested the samples for calcinations above 1000 °C for 2 h; the channel structures collapsed at this high temperature. Therefore, we treated the samples at the range of 700−900 °C in a room air ambient for ∼2 h. SEM images of samples calcined at 115 and 800 °C, respectively, are shown in Figure 2. There are no apparent structural differences between the two samples. The silica particles remain spherical, and the channel structures are well-defined and preserved for treatment at 800 °C for 2 h in air (Figure 2b).

For application in micro- and nanofluidics, the environmental stability of these 1D enclosed channels becomes important. The prepared channeled samples have remarkable mechanical stability, with no apparent degradation with storage in laboratory ambient for long periods (∼months). We also tested the as-prepared channel structures with immersion in water and acetone. Examination of structures before and after immersion in water and acetone (see Figure S1 of the Supporting Information) indicate that the channel structures are robust with no observable degradation for immersion in solvents for a month. In addition, the inner surfaces of the channels are hydrophilic due to the silica particle surface chemistry and the calcination processing. This property will be of benefit for micro- and nanofluidic applications with aqueous-based fluids. The stability of these one-dimensional enclosed structures is more than adequate for many micro- and nanofluidic applications.

Enclosed air cavities and continuous, covered open networks (with nanoparticle pillars holding up nanoparticles

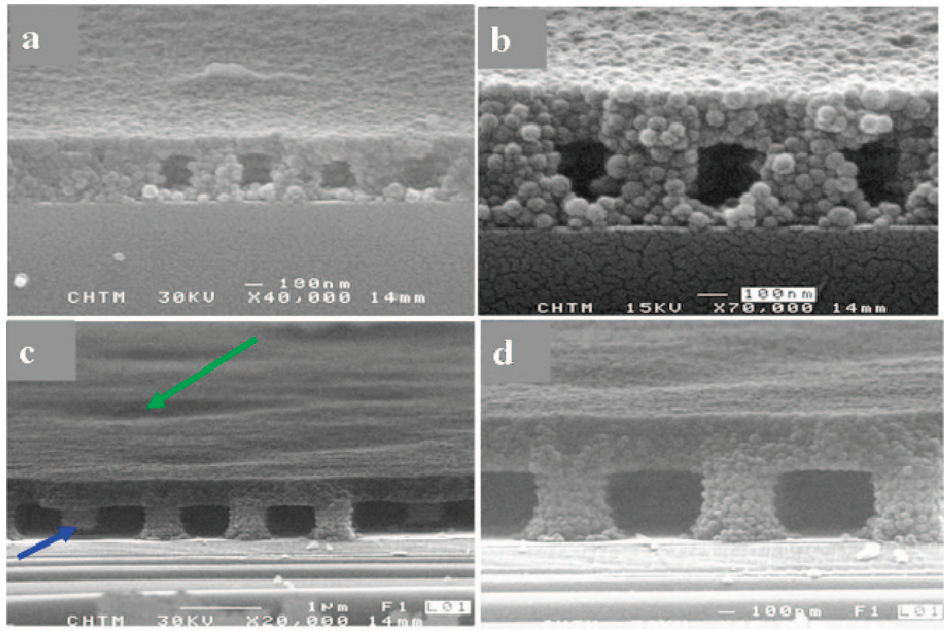

Figure 3. Two-dimensional enclosed structures fabricated with 50 nm silica nanoparticles. (a−b) SEM images of 2D isolated air cavity with 500 nm period and positive PR. (c−d) SEM images of 2D continuous air network with 1000 nm period and negative PR.

roofs) were also easily prepared using this approach, with double exposures in the IL step to produce 2D photoresist patterns as shown in Figure 3. PR posts and holes were produced using positive and negative PR, respectively, in the IL step (see Figure S2 of the Supporting Information). Enclosed isolated air cavities were formed after deposition of silica particles on 2D positive PR/ARC patterns (posts) and removal of PR/ARC by calcination. The PR/ARC post shapes were preserved as air cavities (Figure 3a−b). The existence of isolated air cavities was easily verified by SEM examination of cleaved samples. The left side of the image does not exhibit air cavities, as the cleavage line was not exactly along the center line between the cavities (Figure 3a).

The inverse pattern, a continuous network structure with an upper sealing layer supported by isolated posts, was fabricated with negative PR as shown in Figures 3c−d. As the period of the 2D air-hole patterns increased, the sample fabrication became more successful (see Figure S3 of the Supporting Information for 500 nm period). Images in Figure 3c−d show continuous sealing with isolated posts with a 1 μm period. After spin-coating of silica particle suspension and calcination, the final enclosed structures have broad posts and thick sealing. Even though some posts did not contact the bottom (blue arrow in Figure 3c), the surface flatness and occurrence of defects in the enclosed structures are much improved compared with a 500 nm period structure. In both 500 and 1000 nm period structures, the post heights are shorter than the total thickness of PR/ARC, suggesting that the holes in the PR/ARC pattern were not completely filled during the spin-coating. We investigated thin PR patterns (∼250 nm) with a large period (∼1000 nm) (see Figure S3d of the Supporting Information) to overcome the low uniformity, defects and inconsistency of heights of post and PR/ARC. We investigated the use of smaller silica nanoparticles (∼15 nm diameter), of more dilute silica nanoparticle suspensions, and adjustment of the spin-coating parameters to reduce the defect density without much impact. We examined filled structures after spin-coating and before calcination. The silica nanoparticles only partially filled the holes in the PR/ARC matrix, which resulted in an inconsistency between the heights of the silica posts and PR/ARC (see Figure S4 of the Supporting Information). This variability in filling the PR/ARC holes over a large area likely contributes to defects and nonuniformity of the final film. The partial filling of the holes may be a result of surface hydrophobicity of the isolated air holes in the PR/ARC layer. There is a complex interplay between surface tension and fluid forces during the spin-coating that results in this partial filling of the holes. Compared to the enclosed air cavity structures, the continuous network structure has more defects (for example, shortened posts: blue arrow in Figure 3c) and poorer surface flatness of the top sealing layer (green arrow).

The uniformity of the final enclosed structures depends on the surface wetting properties of the PR pattern surface, PR structures, and silica particle suspension. The success rate and process latitude in forming large-area uniform patterns, from easy to more difficult, is: 1D channel, 2D isolated air cavity, and 2D continuous network. For large spaces around the PR patterns, it is relatively easy for the nanoparticle suspension to flow around the hydrophobic PR obstructions and provide a complete pattern, while small isolated features in the polymer template are more difficult to fill.

The surface wetting properties depend on the micro- and nanostructures and have a complex relationship with the detailed PR structures. For the 1D PR patterned samples, the macroscopic behavior of the colloidal fluid provides a simple diagnostic of the level of filling. For partially filled structures, e.g., colloidal particles below the top of the PR

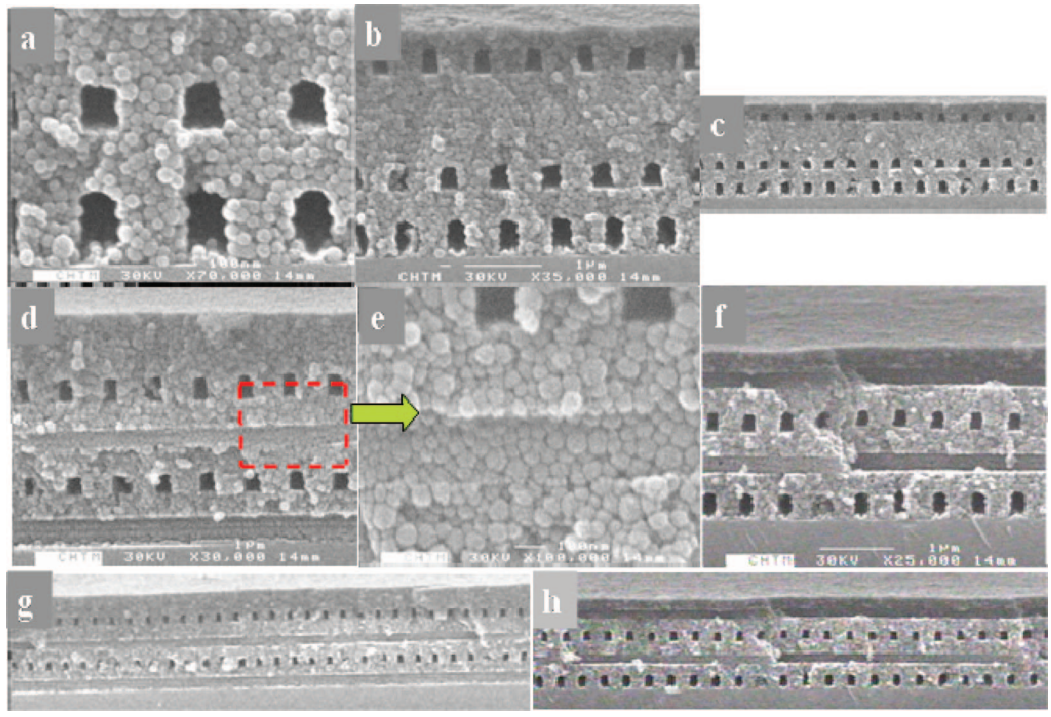

Figure 4. Multiple-layered channels with 500 nm period and 50 nm silica nanoparticles using single-step calcination. (a−c) SEM images of three-parallel layered channels using single-step calcination: (a) enlarged image of bottom two layers; (b) overview of three-layered channels; (c) large area image of three-layered channels. (d−f) SEM images of four perpendicular-layered channels: (d) image from one direction; (e) enlarged image of part of (a); (f) image from orthogonal direction. (g) Large area image of (d). (h) Large area of (f).

lines, the colloidal fluid formed an elongated drop along the direction of the PR lines before spinning. This anisotropic wetting phenomenon was also observed on 1D macropatterned surfaces and explained by Takahara et al.[32] As expected, the 2D symmetry PR patterned surface has more nearly isotropic wetting properties, although faceting along specific symmetry directions of the underlying pattern is still evident for partially filled patterns. We can make use of the anisotropic wetting phenomenon on 1D PR patterns for potential applications in water harvesting surfaces, drug release coatings, open-air nanochannel devices, and laboratory-on-chip integrated structures.[33] The elongation of the drop for the 1D case and the faceting of the edge of the drop along the symmetry lines of the 2D pattern are illustrated in the Supporting Information (see Figure S5 of the Supporting Information). The static contact angles also indicate that the surface wetting properties depend on the period, PR line:space ratio, and PR pattern symmetry. More detailed investigation of the relationship between the PR structures and static contact angles is underway. A thorough understanding of the relationship between PR structures and surface wetting properties will be helpful in improving the uniformity of the resultant enclosed structures prepared with aqueous particle suspensions.

This fabrication approach can be extended to multilayer structures. Previously, we have demonstrated two layer channel samples, fabricated with 50 nm silica nanoparticles, through repeated processing on a single substrate with independent calcinations for each layer.[14] In fabricating multiple-layered enclosed structures, it is more effective to perform a single calcination step following deposition of the complete stack of PR and nanoparticle films. There are two main advantages to the single-step calcination: (1) reduced fabrication time with fewer processing steps and (2) uniform sintering across the multiple layers.

To verify the practicality of single-step calcination, we first fabricated a three-layered parallel channel structure. Three steps of IL and spin-coating of silica particle suspension were followed by a single calcination. We also intentionally deleted one IL step and while still performing the spin-coating between the second and third layer so that the final channel structures are four layers high with three parallel channel layers and a thicker interlevel spacer between the top two channel layers. SEM images of final multiple-layered structures are shown in Figure 4a−c. Three-layered parallel structures with one-dimensional enclosed channels are clearly observed. Even though the same IL parameters were employed in all three steps, the final channel profiles in these three layers were different, mainly due to the varying surface condition of each layer for IL. The upper layer has smaller channel cross sections compared to those in the initial layer. The thicker spacer layer between second and third channel layers is clearly evident.

We also fabricated multiple-layered structures with four channel layers with alternating, orthogonal orientations using a single calcination as shown in Figure 4d−h. The perpendicular channels are observed in Figure 4d−f. The smooth inside wall of channels is obvious from Figure 4e. The open channel cross section over a long length is evident in both directions (Figure 4g−h shows orthogonal perspectives). It is also easy to fabricate multiple-layered stacks with hybrid enclosed structures such as one-dimensional channels in some

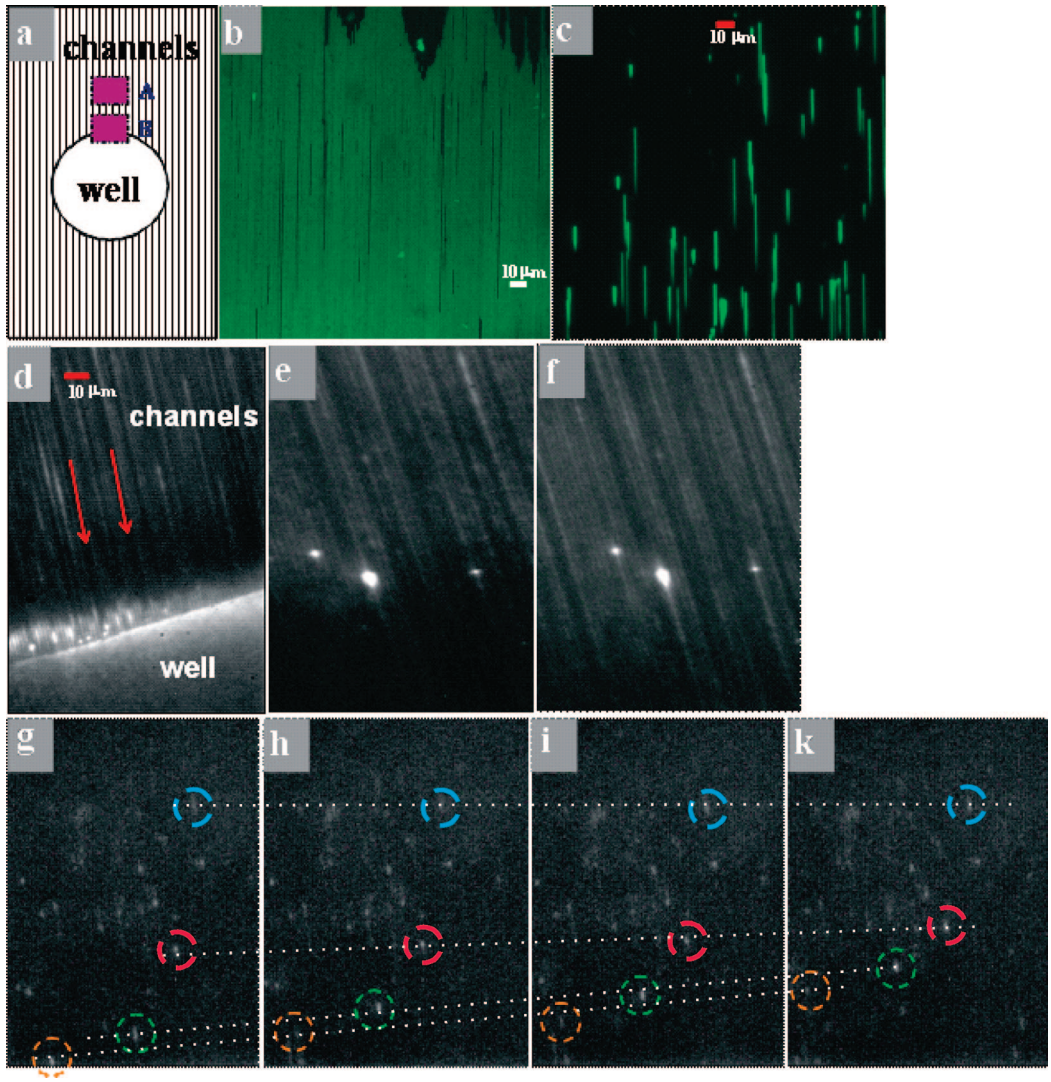

Figure 5. Fluorescent image and DNA extension in 1D channels (500 nm × 600 nm channels, 1200 nm pitch). (a) Schematic of channeled sample with inlet well. (b) Fluorescent dye image in a region far from inlet well. (c) Confocal microscope image of Hind-III digested lambda DNA in region A. (d) Microscope image of DNA in region B just at the edge of well, some channels are blocked (marked by red arrow). (e−f) Microscope image of DNA in region A with 3 s interval. (g−k) Microscope image of DNA using diluted DNA buffer solution (100 times less than in (e) and (f)) in region A with 0.15 s interval (motion of individual DNA molecules marked with colored dashed circles). In all cases, the fluid flow is bottom to top of the image.

layers and two-dimensional air cavities in other layers using single-step calcination.

The as-prepared enclosed structures with nanoparticles have optical applications such as photonic crystals. For example, photonic crystal structures could be fabricated with high refractive index nanoparticles arranged in multiple-layered "Lincoln-log" structures.

Enclosed nanoparticle structures provide the opportunity to fabricate fluidic systems with heterogeneous, hierarchical porosities. We believe enclosed structures will have many applications for catalysis, chemical/biological sensing, and biomolecular separations. Additionally, they may find utility for interconnecting laboratory-on-chip arrays of microfluidic and microreactor devices that perform chemical and catalytic transformations as well as ion, molecule, and macromolecule separations. The continuous network structure with an upper sealing layer supported by isolated posts has potential applications in laboratory-on-a-chip devices; for example, the separation of biological components/molecules and particles by size can be performed through such a connected network with post arrays using laminar fluidic flow.[34] The multiple-layered enclosed structures have applications in separation and detection of biomolecules, efficient bioanalysis by improving separation efficiency (layered enclosed structures), and biomolecular detection sensitivity (large surface area of porous nanochannel structures) as well as concentrating bacteria and viruses in bioanalytical chemistry.

Multiple-layered nanochannels are biomimetic structures akin to the cellular organization of trees, animal skin, bird feathers, and hair.[35,36] The study of nanofluidics in enclosed porous nanochannels will allow investigations of biological processes as well as potentially leading to biomimetic applications.

As an initial illustration of these potential applications, we observed DNA transport in 1D porous nanochannel structures, using capillary action (hydrophilic surface tension)

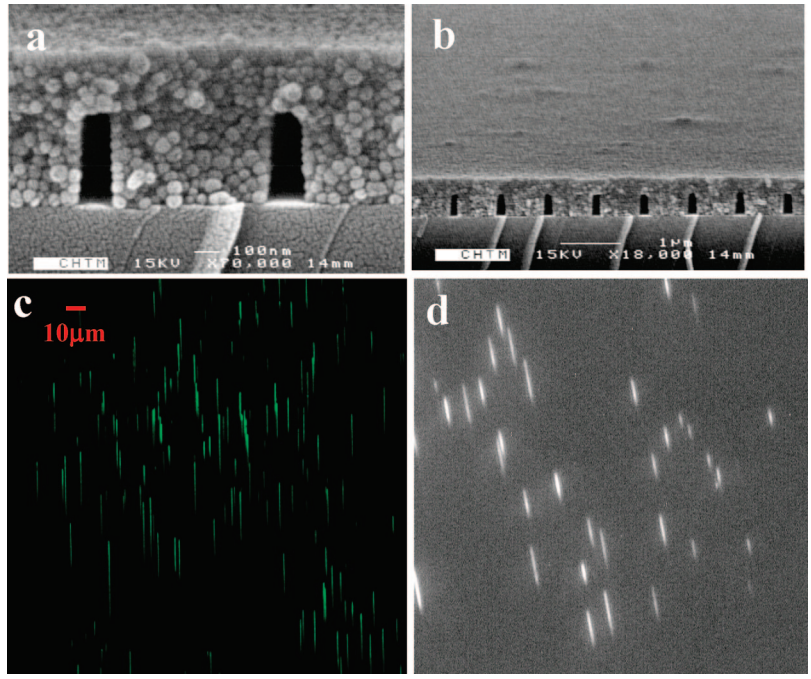

Figure 6. Fluorescent image and DNA extension in narrowed 1D channels (130 nm × 400 nm channels, 800 nm pitch). (a−b) SEM images of channels. (c) Confocal microscope image of DNA in nanochannels. (d) Microscope image of DNA in nanochannels; the fluid flow is bottom to top of the image.

as the driving force. Many reports have explored the use of micro- and nanochannel structures to separate, manipulate, and elongate DNA,[13,37–40] and fabrication techniques for nanofluidic channel devices have been discussed.[41] Compared to previous fabrication approaches, our method has the advantages of ease of fabrication and, importantly for the first time, the provision of interconnected porous structures. We compare the DNA transport in 500 and 130 nm wide nanochannels. First experiments used 500 nm wide porous channels composed of 50 nm silica nanoparticles with a 1200 nm period to test the DNA transport. A circular well was etched for injecting fluorescent dye and/or DNA solution (Figure 5a). To demonstrate the channel continuity over long distances, the 1D channels were filled with DI water containing fluorescent dye by capillary action. Figure 5b shows the fluorescent images captured in a region far from the injecting well. The liquid filled the channels uniformly and continuously. All of the images in Figures 5 and 6 are oriented so that the flow is from bottom to top of the image. In initial investigations, we observed directly a new nanofluidic phenomenon: oscillatory drying/filling in the advancing water fronts in these enclosed porous channels. We attribute this phenomenon to the combination of evaporation through pores between nanoparticles in the sealing layer and capillary driving forces. The oscillatory motion exhibits group behavior, "waves," resulting from communication between adjacent nanochannels by virtue of the porosity.

Fluorescently stained DNA molecules (λ-phage DNA 48.5 kbp, contour length $L = 16.5$ μm, New England Biolabs) were stained with YOYO-1 dye (Molecular Probes) and were readily transported into 500 nm wide porous channels using capillary filling. Figure 5c shows a confocal microscopy image of aligned DNA filling the individual nanochannels in long streaks. This image was taken in region A, indicated in Figure 5a. The optical resolution is insufficient to resolve any transverse structure. The uniform intensity and similar lengths are reminiscent of aligned DNA molecules.[13] However, the apparent lengths (20−50 μm) are longer than the known contour length of these polymers in channels of comparable size (~2 μm),[42] so there must be some clustering of the DNA molecules (perhaps concatamers of the self-cDNA molecules). Without extra forces, the capillary driven motion of DNA reaches as far as several hundreds of micrometers from the well, limited by the evaporation of the fluid through the porous tops. Figure 5d shows a video frame capture of the fluorescence just at the interface between the well and the nanochannels (region B in Figure 5a). This image was taken after the initial filling of the nanochannels. Continuous drying by evaporation from the porous tops of the nanochannels and refilling from the reservoir provides continuous additions and flow of DNA into and within the channels. There are several interesting observations: (1) there is clearly a cooperative effect between channels because the DNA just at the channel edges proceeds in a "wave" that is consistent across many channels, and this is likely a result of the porous sidewalls that ensure a uniform fluid pressure across the channels; (2) the fluorescent intensity varies significantly within different nanochannels, again suggesting some aggregation of individual DNA molecules in these relatively wide channels; (3) there is a clearly discernible, but unresolved, fluorescent glow just at the entrance to the nanochannels from additional DNA molecules that are "stacked up" at the channel entrances; (4) the length of the fluorescent streaks associated with highly mobile DNA, the short streaks just inside the channels, is much shorter than the relatively immobile fluorescence sources corresponding

to the long streaks in Figure 5d, which are likely the same as those in Figure 5c; (5) there are some blocked channels with no fluorescence, and some of these are indicated by the red arrows in the Figure 5d.

The DNA velocities are clearly a function of position and of previous filling cycles. The DNA motion on initial filling of dry channels is so rapid that we could not resolve the individual DNA molecules with standard frame rates. After several cycles of filling, the DNA molecules accumulate into bright lines in the top half of the images (further from the well), reflecting increased concentration of the DNA. As the DNA motion continues, the edge of the region of bright lines moves down as seen in Figure 5f. Using a diluted DNA buffer solution, we easily observe the motion of individual DNA molecules as shown in Figure 5g−k. The dotted lines follow individual DNA molecules across four consecutive frames. Clearly, the velocities are slowing as the particles reach the top of the field, representing a clear concentration enhancement. Even though we still observe the accumulation of DNA toward the middle of each image, the density and brightness are much lower. An important observation is that we can readily view the motion of individual DNA molecules as marked with the colored circles. The two lowest DNA molecules (orange and green circles) move up toward the "stationary region" at the same speed, while the motion of the DNA molecules in the middle of the image (red circles) is slower, and it is imperceptible at the top of the image (blue circles). The length of observed single DNA in images is around 2 μm, similar to previous literature reports in the same scale of nanochannels.[42,43] The sidewall porosity among the 1D channels provides the communication between the channels as shown in the "wave" in Figure 5d and in the correlated motion within different channels shown in Figure 5g−k.

With current fabrication approaches, we are able to readily fabricate porous nanochannels with smaller cross sections. Smaller silica nanoparticles (e.g., 15 nm) can be employed to fabricate porous nanochannels with widths less than 100 nm.[44] Even with 50 nm silica nanoparticles, we were able to fabricate porous nanochannels with widths of ~100 nm as shown in Figure 6. The images in parts a and b of Figure 6 show as-prepared nanochannels (fabricated with positive photoresist, which enables narrower photoresist widths) with a 130 nm wide and 400 nm high cross section and a 800 nm pitch. DNA transport behavior was investigated in these samples as well. The DNA was less likely to enter these smaller channels and moved more slowly. With only capillary forces, the DNA molecules are transported only a short distance into the channels as compared to the above 500 nm wide channels. The apparent length of the concatamer DNA arrays (15−25 μm) is shorter in these channels as shown in Figure 6c compared to Figure 5c. The dimensions of the channels clearly affected the static and dynamical behaviors of the DNA.[43] The real-time microscope image further confirmed the streaks of DNA confined in nanochannels (Figure 6d). The fluorescence from individual DNA molecules in images captured in a video frame is rather faint (see Figure S6 of the Supporting Information) as a result of bleaching, the rapid motion of the DNA, and instrumental limitations. With the successful fabrication of porous nanochannels over a wide size range, further efforts are underway to investigate the detailed transport mechanisms, effect of channels size and DNA types, and DNA solution environments such as ionic strength.[43]

The fabrication of hierarchically enclosed nanostructures in colloidal particle films opens new directions in the preparation of unique, biomimetic porous enclosed structures with many potential applications. Various enclosed structures, which include channels, isolated air cavities, continuous networks, and multiple-layered channels buried in colloidal particle films, were successfully demonstrated with this simple approach. The resultant enclosed structures have excellent mechanical strength, high environmental stability, good uniformity, and proven ability to transport aqueous solutions and large organic macromolecules such as DNA. The multiple layered channels are biomimetic structures akin to the cellular organization of trees, animal skin, feathers, and hair. They are an attractive platform for the study of natural processes and can be engineered for many biomimetic applications including fluidics, biomolecular separation and sensing, detection, and catalysis.

Acknowledgment. Partial support for this work was provided by the NSF (IIS 0515684 and CTS 0404124) and by the Army Research Office under a subcontract from Redondo Optics, Inc.

Supporting Information Available: Experimental details and supporting SEM images. This material is available free of charge via the Internet at http://pubs.acs.org.

References

(1) Velev, O. D.; Tessier, P. M.; Lenhoff, A. M.; Kaler, E. W. *Nature* **1999**, *401*, 548.
(2) Jiang, P.; J. Bertone, F.; Colvin, V. A. *Science* **2001**, *291*, 453–457.
(3) Lahav, M.; Sehayek, T.; Vaskevich, A.; Rubinstein, I. *Angew. Chem., Int. Ed.* **2003**, *42*, 5576–5579.
(4) Hong, S. H.; Moon, J. H.; Lim, J.-M.; Kim., S.-H.; Yang, S.-M. *Langmuir* **2005**, *21*, 10416–10421.
(5) Moon, J. H.; Kim, S.; Yi, G.-R.; Lee, Y.-H.; Yang, S.-M. *Langmuir* **2004**, *20*, 2033–2035.
(6) Yi, G.-R.; Manaharan, V. N.; Klein, S.; Brzezinska, K. R.; Pine, D. J.; Lange, F. F.; Yang, S.-M. *Adv. Mater.* **2002**, *14*, 1137–1140.
(7) Iskandar, F.; Mikrajuddin; Okuyama, K. *Nano Lett.* **2002**, *2*, 389–392.
(8) Li, Q.; Lewis, J. A. *Adv. Mater.* **2003**, *15*, 1639–1643.
(9) Zaumseil, J.; Eitl, M. A.; Hsu, J. E. P.; Acharya, B. R.; Baldwin, K. W.; Loo, L.-Y.; Roger, J. A. *Nano Lett.* **2003**, *3*, 1223–1227.
(10) Jeon, S.; Menard, E.; Park, J.-U.; Maria, J.; Meitl, M.; Zaumseil, J.; Roger, J. A. *Adv. Mater.* **2004**, *16*, 1369–1373.
(11) Lee, C.; Yang, E. H.; Myung, N. V.; George, T. A. *Nano Lett.* **2003**, *3*, 1339–1340.
(12) Brien, J. O., II; Bisong, P.; Ista, L. K.; Rabinovich, E. M.; Garcia, A. L.; Sibbett, S. S.; Lopez, G. P.; Brueck, S. R. J. *J. Vac. Sci. Technol., B* **2003**, *21*, 2941–2945.
(13) Cao, H.; Yu, Z.; Wang, J.; Tegenfeldt, J. O.; Austin, R. H.; Wu, W.; Chou, S. Y. *Appl. Phys. Lett.* **2002**, *81*, 174–176.
(14) Xia, D.; Brueck, S. R. J. *J. Vac. Sci. Technol., B* **2005**, *23*, 2694–2699.
(15) Gates, B.; Xu, Q.; Stewart, M.; Ryan, D.; Willson, C. G.; Whitesides, G. M. *Chem. Rev.* **2005**, *105*, 1171–1196.
(16) Wang, D.; Mohwald, H. *J. Mater. Chem.* **2004**, *14*, 459–468.
(17) Xia, D.; Biswas, A.; Li, D.; Brueck, S. R. J. *Adv. Mater.* **2004**, *16*, 1427–1432.

(18) Xia, D.; Brueck, S. R. J. *Nano Lett.* **2004**, *4*, 1295–1299.
(19) Brueck, S. R. J. *Proc. IEEE* **2005**, *93*, 1704–1721.
(20) Campbell, M.; Sharp, D. N.; Harrison, M. T.; Denning, R. G.; Turberfield, A. J. *Nature* **2000**, *404*, 53–56.
(21) Zhang, S.; Fan, W.; Frauenglass, A.; Minhas, B.; Malloy, K. J.; Brueck, S. R. J. *Phys. Rev. Lett.* **2005**, *94*, 037402.
(22) Zhang, S.; Fan, W.; Panoiu, N. C.; Malloy, K. J.; Osgood, R. M.; Brueck, S. R. J. *Phys. Rev. Lett.* **2005**, *95*, 137404.
(23) Yan, Q.; Zhou, Z.; Zhao, X. S.; Chua, S. J. *Adv. Mater.* **2005**, *17*, 1917–1920.
(24) Vekris, E.; Kitaev, V.; von Freymann, G.; Perovic, D. D.; Aitchison, J. S.; Ozin, G. A. *Adv. Mater.* **2005**, *17*, 1269–1272.
(25) Xia, D.; Li, D.; Luo, Y.; Brueck, S. R. J. *Adv. Mater.* **2006**, *18*, 930–933.
(26) Xia, D.; Li, D.; Ku, Z.; Luo, Y.; Brueck, S. R. J. *Langmuir* **2007**, *23*, 5377–5385.
(27) McLellan, J. M.; Geissler, M.; Xia, Y. *J. Am. Chem. Soc.* **2004**, *126*, 10830–10831.
(28) Wong, S.; Kitaev, V.; Ozin, G. A. *J. Am. Chem. Soc.* **2003**, *125*, 15589–15598.
(29) Schweigert, I. V.; Lehtinen, K. E. J.; Carrier, M. J.; Zachariah, M. R. *Phys. Rev. B* **2002**, *65*, 235410.
(30) Sacks, M. D.; Seng, T. Y. *J. Am. Ceram. Soc.* **1984**, *67*, 532–537.
(31) Miguez, H.; Meseguer, F.; Lopez, C.; Blanco, A.; Moya, J. S.; Requena, J.; Mifsud, A.; Fornes, V. *Adv. Mater.* **1998**, *10*, 480–483.
(32) Morita, M.; Koga, T.; Otsuka, H.; Takahara, A. *Langmuir* **2005**, *21*, 911–918.
(33) Zhai, L.; Berg, M. C.; Cebeci, F. C.; Kim, Y.; Miwid, J. M.; Rubner, M. F.; Cohen, R. E. *Nano Lett.* **2006**, *6*, 1213–1217.
(34) Davis, J. A.; Inglis, D. W.; Morton, K. J.; Lawrence, D. A.; Huang, L. R.; Chou, S. Y.; Sturm, J. C.; Austin, R. H. *Proc. Natl. Acad. Sci. U. S. A.* **2006**, *103*, 14779–14784.
(35) Hungate, R. E. *Plant Physiol. D* **1934**, *9*, 783–794.
(36) Zhao, Y.; Cao, X.; Zhang, L. *J. Am. Chem. Soc.* **2007**, *129*, 764–765.
(37) Han, J.; Graighead, H. G. *Science* **2000**, *288*, 1026–1029.
(38) Dukkipati, V. R.; Pang, S. W. *Appl. Phys. Lett.* **2007**, *90*, 083901.
(39) Huh, D.; Mills, K. L.; Zhu, X.; Burns, M. A.; Thouless, M. D.; Takayama, S. *Nat. Mater.* **2007**, *6*, 424–428.
(40) Liang, X.; Morton, K. J.; Austin, R. H.; Chou, S. Y. *Nano Lett.* **2007**, *7*, 3774–3780.
(41) Mijatovic, D.; Eijkel, J. C. T.; van den Berg, A. *Lab Chip* **2005**, *5*, 492–500.
(42) Reisner, W.; Morton, K. J.; Riegn, R.; Wang, Y. M.; Yu, Z.; Rosen, M.; Sturm, J. C.; Chou, S. Y.; Frey, E.; Austin, R. H. *Phys. Rev. Lett.* **2005**, *94*, 196101.
(43) Reisner, W.; Beech, J. P.; Larsen, N. B.; Flyvbjerg, H.; Kristensen, A.; Tegenfieldt, J. O. *Phys. Rev. Lett.* **2007**, *99*, 058302.
(44) Xia, D.; Brueck, S. R. J. *J. Vac. Sci. Technol., B* **2004**, *22*, 3415–3420.

NL080190S